

# Weakly supervised anomaly detection with event-level variables

Liam Brennan,<sup>1,\*</sup> Tamas Almos Vami,<sup>1,†</sup> Oz Amram,<sup>2,‡</sup> Sanjana Sekhar,<sup>3</sup> Yuta Takahashi,<sup>4</sup> Louis Moureaux,<sup>5</sup> Manuel Sommerhalder,<sup>5</sup> Petar Maksimovic,<sup>3</sup> and Tianji Cai<sup>6</sup>

<sup>1</sup>*University of California Santa Barbara, Santa Barbara, CA, USA*

<sup>2</sup>*Fermilab, Batavia, IL, USA*

<sup>3</sup>*Johns Hopkins University, Baltimore, MD, USA*

<sup>4</sup>*University of Florida, Gainesville, FL, USA*

<sup>5</sup>*University of Hamburg, Hamburg, Germany*

<sup>6</sup>*SLAC National Accelerator Laboratory, Menlo Park, CA, USA*

We introduce a new topology for weakly supervised anomaly detection searches, di-object plus X. In this topology, one looks for a resonance decaying to two standard model particles produced in association with other anomalous event activity (X). This additional activity is used for classification. We demonstrate how anomaly detection techniques which have been developed for di-jet searches focusing on jet substructure anomalies can be applied to event-level anomaly detection in this topology. To robustly capture event-level features of multi-particle kinematics, we employ new physically motivated variables derived from the geometric structure of a collision's phase space manifold. As a proof of concept, we explore the application of this approach to several benchmark signals in the di- $\tau$  plus X final state. We demonstrate that our anomaly detection approach can reach discovery-level significances for signals that would be missed in a conventional bump-hunt approach.

## I. INTRODUCTION

Despite many searches for new particles at the Large Hadron Collider (LHC), no clear evidence of beyond standard model physics (BSM) has been found. However, the space of possible signals which could be hiding in LHC data far exceeds the coverage of the dedicated searches performed thus far. In recent years, anomaly detection has been proposed as a new paradigm for conducting searches at the LHC [1–3]. Rather than designing a search to target a specific signal model, anomaly detection analyses take a model-agnostic approach. They use novel machine-learning-based strategies to identify events which differ from typical backgrounds without reference to a specific signal. Both the ATLAS and CMS collaborations have now released searches involving these new anomaly detection approaches [4–8] and additional studies have been performed using CMS open data [9, 10].

The majority of proposed anomaly detection algorithms can generally be split into two separate categories: unsupervised and weakly supervised algorithms. Unsupervised algorithms, first proposed in Refs. [11, 12], are trained solely on background events and are then used to define an anomaly score which quantifies how similar an input event is to typical background events. Weakly supervised methods build on the classification without labels paradigm [13] to learn to distinguish between signal and background. This is accomplished by training a classifier to distinguish events in the signal region (SR), which may contain some small fraction of signal, from a carefully constructed sample of background-only

events [14, 15]. Weakly supervised methods have the advantage that they are asymptotically optimal: the optimal weakly supervised classifier will learn the likelihood ratio, which is the ideal signal versus background classifier.

Because weakly supervised algorithms need a high-quality estimate of the background in a high-dimensional space, their applications have mostly focused on resonant signals, so the background composition in a signal mass window can be learned through an interpolation from sideband regions. Several approaches have been proposed to achieve the necessary high-quality background estimate [14–23]. The majority of these first anomaly detection approaches have focused on heavy resonances decaying to two boosted large radius jets, where well-studied jet substructure observables, with minimal correlations with the resonance mass, can be used as the classification features. There is also a large space of signal models which could produce many phenomenological varieties of jets, making this topology ideal for anomaly detection. However, considerably less effort has been put into exploring other signal topologies which could work with a weakly supervised resonant anomaly detection approach.

Several works have studied the application of anomaly detection methods to topologies beyond di-jet resonances. Refs. [24, 25] studied the application of weak supervision to topologies with high missing energy and a boosted jet. Ref. [26] studied the application of CATHODE to supersymmetry scenarios producing pairs of gluinos. Recently, Ref. [10] applied the CATHODE method to CMS open data to demonstrate the identification of  $\Upsilon$  particles decaying to muon pairs. This study used only features related to the dimuon resonance for classification rather than focusing on the other event activity we exploit here. A previous ATLAS search [6] applied an event-level unsupervised autoencoder-based

\* [Liam.Robert.Brennan@cern.ch](mailto:Liam.Robert.Brennan@cern.ch)

† [Tamas.Almos.Vami@cern.ch](mailto:Tamas.Almos.Vami@cern.ch)

‡ [Oz.Amram@cern.ch](mailto:Oz.Amram@cern.ch)

anomaly detection algorithm to search for resonances for several di-object combinations, where at least one of the objects was required to be a jet.

In this paper, we explore the application of weakly supervised anomaly detection in a new di-object + X topology using the CATHODE methodology [18] with event-level features. We consider signals which produce a two-body resonance in addition to other particles (X). Such a signature can easily arise if the resonance is produced through an extended decay chain or from associated production with additional particles. These production mechanisms can lead to striking experimental signatures, with many objects in the event, potentially with rich kinematic correlations, and/or high missing energy. These distinct signatures can be leveraged to significantly reduce backgrounds; however, given the large phenomenological space of possibilities it is infeasible to design analysis strategies for every possible scenario. These two factors make for an ideal application of anomaly detection methods. This work develops a general framework for weakly supervised searches using event-level classification. The usage of weakly supervised, rather than unsupervised, anomaly detection may also offer larger discovery potential for anomalies due to improved classification performance [27].

As a first exploration of this general topology, this work focuses specifically on the scenario where the resonance decays into two  $\tau$  leptons. Searches featuring  $\tau$  leptons are strongly motivated by various BSM theories, which often preferentially couple to third-generation fermions, but are less explored at the LHC due to their more complex experimental signatures. Examples of searches include  $Z'$  bosons [28], leptoquarks [29–31], and additional Higgs bosons [32, 33]. These new particles are motivated by the observed anomalies in  $B$ -hadron decays to  $D^{(*)}\tau\nu$ , which show enhanced rates compared to the corresponding decays involving lighter leptons [34–42]. If these anomalies are caused by heavy BSM particles, it is likely they also influence the di- $\tau$  production at high invariant masses.

Though we focus on the di- $\tau$  final state in this work, the methodology we develop is entirely general and is applicable to other resonance + X searches, such as di-muon, di-electron, di-photon, or di-jet resonance + X. Although these other final states may have somewhat better existing experimental coverage, there is almost certainly still unexplored ‘X’ signatures which could be covered by our approach. These other final states may also offer the advantage of larger samples available for the training of the background model of the CATHODE method which can improve performance.

The simulated data used in this paper can be found under Refs. [43, 44] and the analysis code is available on GitHub [45].

## II. SETUP

In this study, we focus on the final state where both  $\tau$  leptons decay hadronically, which is the decay mode with the largest branching ratio. Unlike di-jet searches where the QCD multijet background is dominant, di- $\tau$  searches receive considerable backgrounds from multiple physics processes. The dominant backgrounds in the all hadronic final state are Drell–Yan and  $t\bar{t}$ . QCD and W+jets also contribute in this channel, with the fraction dependent on the purity of the  $\tau$  identification criteria being employed and pre-selection requirements. As this is an exploratory work, and these effects are not modeled well with simulation, we focus here on the Drell–Yan and  $t\bar{t}$  backgrounds only. The methodology we employ should generally account for any background which varies smoothly in di- $\tau$  mass. Due to the multiple decay modes of the  $\tau$  and limited reconstruction efficiencies, di- $\tau$  searches feature significantly smaller event samples than the di-jet searches of prior weakly supervised searches. This presents an interesting challenge for the application of weakly supervised methods which require a large sample of background events in order to properly learn the probability distribution of the background events.

We apply the CATHODE method for resonant anomaly detection [18]. In CATHODE one defines a resonant variable, in our case the visible mass of the di- $\tau$  candidate,  $m_{\text{vis}}$ , and a set of features to be used for classification,  $\vec{x}$ . Signals are assumed to manifest in a localized region of the resonant variable, allowing the probability distribution of the background to be learned from neighboring sideband regions. The method proceeds in two steps. First, a generative model is trained on the sideband regions to learn the probability density of  $\vec{x}$  conditioned on  $m_{\text{vis}}$  for the background,  $P_b(\vec{x}|m_{\text{vis}})$ . The trained generative model is then interpolated into the signal region and used to generate synthetic background events. A weakly supervised classifier is then trained to distinguish between the real data events  $p_{\text{data}}(\vec{x})$  in the signal region and the synthetic background events  $p_{\text{bkg}}(\vec{x})$ . If there is a true signal in the signal region abundant in sufficient quantity, then the classifier will learn to identify its events, which will look anomalous with respect to the interpolated background.

The application of weak supervision to event-level anomaly detection raises interesting choices in feature selection. Weak supervision is typically performed with a moderately-sized set of high-level features, and its performance is known to deteriorate with the use of many uninformative features [46]. Due to the noise inherent to the weakly supervised training objective, the use of lower-level, higher-dimensional representations of the event can struggle to achieve good classification performance for moderate strength signals [47]. Though this degradation may be mitigated in the classification step through the use of boosted decision trees as opposed to neural networks [46, 48], using a very high-dimensional feature set may cause difficulties in learning an accurate background

estimate given the limited size of the training set available in final states such as  $\text{di-}\tau$ .

For these reasons, we explore the usage of the recently introduced [49, 50] phase space variables to encode the relevant kinematic features of the event in a compact representation. In Ref. [50] a covariant description of the phase space of collider events producing a chosen number ( $N$ ) of massless final-state particles was presented. The manifold of this  $N$ -body phase space,  $\Pi_N$ , was shown to be isomorphic to the product of an  $(N-1)$ -simplex ( $\Delta_{N-1}$ ) and a  $(2N-3)$ -hypersphere ( $S_{2N-3}$ ), i.e.  $\Pi_N \cong \Delta_{N-1} \times S_{2N-3}$ . A set of explicit and global coordinates of the phase space have been introduced:  $(N)$   $\rho$  coordinates on the simplex  $\Delta_{N-1}$  and  $(N-1)$  complex  $\xi$  coordinates on the hypersphere  $S_{2N-3}$ . Ref. [50] used this representation to develop a distance metric between events produced at a hadron collider using these global phase space coordinates. In this work, we do not use this distance metric, but rather directly use the phase space coordinates as a way to represent the kinematics of all the final state objects in the event. We exploit the simplex coordinates only, since we found that the normalizing flows used for the background model, described in Section IV, have difficulties with the non-trivial topology of the hypersphere coordinates.

It should be noted that the phase space coordinates encode only the kinematics of the event, and therefore, do not capture all event features that may be useful for event-level anomaly detection. For example, they do not encode which type of object in the event (jet, lepton, photon, etc) is producing said kinematics. It therefore may be useful to supplement phase space variables with additional variables which encode object-type information. The phase space variables are also normalized such that they depend only on the relative fraction of energies carried by each object and its orientation. They do not contain information about the overall energy scale of the event; i.e. an event with 100 GeV of energy split evenly among 10 jets in a certain topology is encoded the same as an event with 1 TeV split among those jets in the same topology. We therefore supplement such scale information to our feature set used for classification.

### III. SIMULATED SAMPLES

We produced simulated samples with **MadGraph\_aMC@NLO** [51] v3.5.4 using **UFOs** [52] from the **FeynRules** database. We set the center of mass energy to 13 TeV in order to match the Run-2 conditions of the LHC. Hadronization was done with **Pythia8** [53] v8.306. All samples are generated at leading order using the NNPDF2.3 LO parton distribution function [54, 55], with default dynamic scale choices in **MadGraph**.

For the SM background samples we used the SM **UFO** [56] with CKM mixing, and with the four-flavor scheme. We simulated extra jets (ISR/FSR) up to 2 jets, i.e. 0, 1, or 2 jets besides the hard scatter. Ma-

trix element and parton shower matching was performed using the MLM scheme [57] with a matching scale of 30 GeV. For the  $t\bar{t}$  sample, the top quarks were decayed in **MadSpin** [58] to W bosons that decay to  $\tau$  leptons. In order to enhance the generation efficiency, we applied a generator level cut on the  $\text{di-}\tau$  invariant mass of 120 GeV. The cross section of the Drell-Yan sample is 17.37 pb and the cross section of the  $t\bar{t}$  sample is 13.49 pb. Sufficient events were generated to have an equivalent luminosity of  $138 \text{ fb}^{-1}$ , to match that of the proton-proton collisions data taken during Run-2 (2016-18) of the LHC.

We explored a set of several BSM models as benchmarks to evaluate the performance of our approach. The details of the generation are summarized in Table I, where the number of events is after the generator cuts are applied. Some example Feynman diagrams of the signal processes are shown in Fig. 2. For simplicity, we set the masses of the  $\text{di-}\tau$  resonance in all models to 250 GeV.

In the 2HDM model [59–61] we use the heavy Higgs particle, denoted with  $\Phi$ , and let it decay to a  $\tau$  lepton pair. In the eVLQ model [62, 63], we let the vector-like quark,  $T'$  decay to a SM top and a BSM scalar  $S^0$ . One of the  $S^0$  then decays to a  $\tau$  lepton pair while the other decays inclusively according to branching ratios similar to a heavy Higgs boson. In the NMSSM model [64–68] we simulate cascade processes, where the heavy resonance X decays to a Higgs boson (H) and an unknown particle Y. Y further decays to the  $\tau$  pair and the H decays invisibly, leading to missing transverse momentum. We explored non-resonant signals such as vector-like anti-leptons [69], leptoquarks [70] and heavy neutral leptons [71]. We did not achieve significant improvements with our method on these signals, as expected since these models are not well localized to the signal region, making them difficult to identify with the CATHODE approach. We therefore did not study them further.

We used **Delphes** [72] to simulate detector and reconstruction effects, using the **CMS** detector settings. Jets were clustered using the anti- $k_T$  algorithm with  $R = 0.4$  as implemented in **FastJet** [73] via **Delphes**.  $\tau$  jets were reconstructed using the default CMS **Delphes**  $\tau$  tagging module with  $p_T > 20 \text{ GeV}$  and  $|\eta| < 2.5$ . A 1% rate of mis-tagging QCD jets as  $\tau$ 's and a 60%  $\tau$  tagging efficiency were included [74, 75]. No dedicated trigger simulation was included.

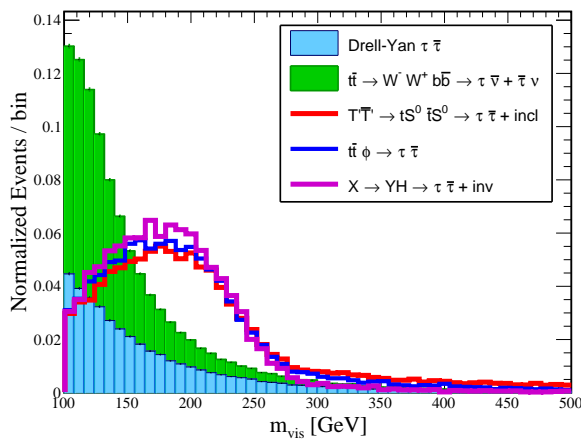
Figure 1 shows the reconstructed invariant visible mass distribution of the  $\text{di-}\tau$  system. While the generator level mass cut is at 120 GeV, because some of the  $\text{di-}\tau$  momentum is lost to the neutrinos, the reconstructed visible mass peaks at 100 GeV. Histograms are normalized to unit area.

### IV. METHODS

We select the two highest  $p_T$   $\tau$ -tagged jets with  $|\eta| < 2.4$  as our resonance candidate. The leading  $\tau$  jet is required to have  $p_T > 40 \text{ GeV}$ . We use the  $m_{\text{vis}}$  as our

UFO	Name	Extra jets	Parameters	#Events
SM	Drell–Yan $\tau\bar{\tau}$	up to 2	N/A	3M
SM	$t\bar{t} \rightarrow W^- W^+ b\bar{b} \rightarrow \tau\bar{\nu} + \bar{\tau}\nu$	up to 2	N/A	2M
2HDM	$t\bar{t}\Phi \rightarrow \tau\bar{\tau}$	0	$m_\Phi = 250 \text{ GeV}$	100k
eVLQ	$T'\bar{T}' \rightarrow tS^0\bar{t}S^0 \rightarrow \tau\bar{\tau} + \text{incl}$	0	$m_{T'} = 1000 \text{ GeV}$ $m_S = 250 \text{ GeV}$	100k
NMSSM	$X \rightarrow YH \rightarrow \tau\bar{\tau} + \text{inv}$	0	$m_X = 800 \text{ GeV}$ $m_H = 400 \text{ GeV}$ $m_Y = 250 \text{ GeV}$	100k

TABLE I. List of samples used, and the details of the production.

FIG. 1. Invariant visible mass distribution of the di- $\tau$  system.

resonance variable in the CATHODE approach and require  $m_{\text{vis}} > 100 \text{ GeV}$ . For simplicity, we consider a single signal region (SR) with a mass window of 175–300 GeV, which contains the majority of our generated signals, as visible in Fig. 1. In a real search, a scan could be performed repeating the procedure for different signal window choices to cover the full range as has been done in previous anomaly detection searches.

Within the SR, we reserve 15% of background events as a test set for performance evaluation and an equal number of signal events. The remaining 85% of SR background events were divided equally between training (42.5%) and validation (42.5%) sets. In a true search, a cross-validation approach would be employed to ensure data events are not reused for training and signal extraction, as had been done in prior weakly supervised searches [4, 7, 8]. Signals are injected into the SR with varying strengths to test performance, as discussed in Sec. V.

### A. Features

To establish a consistent representation of the phase space manifold, we require fixed dimensionality of objects across all events. We define events in terms of constituent objects (jets, electrons, muons, or photons), with each event represented by exactly fifteen objects. For events with fewer than fifteen physical objects, we perform zero-padding with four-vectors as  $(E, p_x, p_y, p_z) = (0.1, 0.1, 0, 0)$ . Objects are ordered by decreasing transverse momentum ( $p_T = \sqrt{p_x^2 + p_y^2}$ ) to ensure consistent event representation.

The fifteen objects yield fifteen simplex coordinates per event, following the manifold construction described in Section II. Our analysis reveals that the first ten simplex coordinates capture the majority of the relevant phase space topology, with the remaining coordinates primarily corresponding to the zero-padded objects in typical events.

To complement the phase space variables, we incorporate event-level kinematic observables: the scalar sum of non- $\tau$  jet  $p_T$ , the missing transverse momentum (MET), and the angular separation ( $\Delta R = \sqrt{(\Delta\eta)^2 + (\Delta\phi)^2}$ , where  $\eta$  is the pseudorapidity and  $\phi$  is the azimuthal angle) between the two  $\tau$  jets. These features encode global event characteristics that are not fully captured by the phase space coordinates alone. Our final feature vector consists of: the first ten simplex coordinates, MET, non- $\tau$  jet  $p_T$  sum, and di- $\tau$   $\Delta R$ .

Because of the unique characteristics of the phase space coordinates, it was found to be necessary to add a small amount of noise to the zero-padded phase space coordinates so that they could be well simulated by the generative model. Details of this preprocessing are given in Appendix 1.

### B. Classification and Background Evaluation

Our generative model uses a normalizing flow architecture based on rational quadratic splines [76], and is

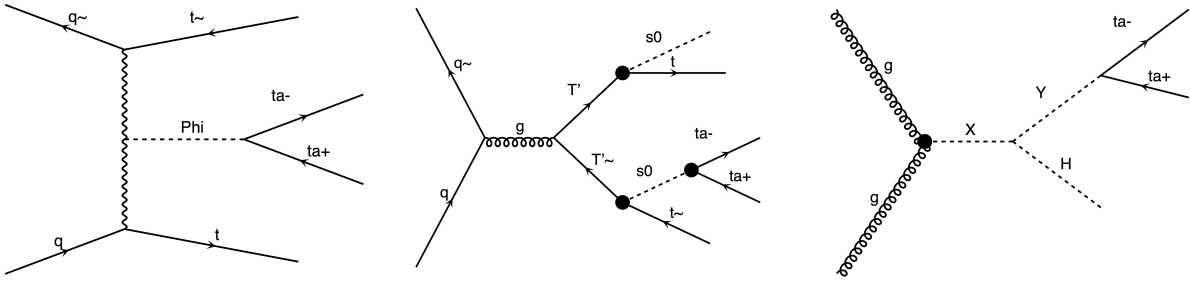


FIG. 2. Feynman diagrams of the  $t\bar{t}\phi$  (left),  $T'\bar{T}'$  (middle), and  $X \rightarrow YH$  (right) signal models. The  $\tau\bar{\tau}$  symbol denotes the  $\tau$  leptons, and  $\sim$  is used to denote the anti-particles. The  $S^0$  decays inclusively according to its branching ratios. The  $H$  boson in the  $X \rightarrow YH$  model decays invisibly.

trained in the sidebands. For simplicity, the training is performed on a background-only sideband sample, assuming the signal contamination to be negligible. A kernel density estimate is used to learn the  $m_{\text{vis}}$  distribution for use in synthetic background generation. Details of the model architecture and exact generation procedure are given in Appendix 2.

After training, we oversample events from the background model to generate synthetic background events in the SR at 3 times the amount of data in the SR. This oversampling provides the classifier with additional background examples to learn from, improving the robustness of the weakly supervised classification. Class balance is maintained through an appropriate weighting in the loss function.

For the weakly supervised classification task, we employ an ensemble of 50 histogram-based gradient boosted decision trees (BDTs). Ensembles of BDTs have demonstrated superior performance over neural networks in weakly supervised training with high-dimensional feature spaces [46]. Our implementation utilizes the `HistGradientBoosting` classifier from `scikit-learn` [77].

Once we have trained the weakly-supervised classifier, we define our final event selection based on a cut on the classifier score that is 1% efficient on the background. Though tighter cuts are seen to yield higher signal enhancements, this threshold is seen to give good classification performance for all signals, and is realistic to thresholds used in previous weakly supervised anomaly detection searches [4, 7, 8].

### C. Synthetic Background Quality Validation

A comparison of the synthetic events generated by the background model and the true background events in the SR is shown in Fig. 3.

The synthetic events mimic the background relatively well, besides some residual discrepancies seen for the lower values of each distribution. Normalizing flows are known to have difficulties modeling sharp features near the edges of distributions. As this region of phase space

is the most background-dominated, its mismodeling may have a reduced impact on signal identification performance.

To validate the quality of our synthetic background, we applied our BDT classifier to distinguish real background events from synthetic ones. This process yields a classification area under curve of 0.55, close to the random-chance value of 0.5. Imperfect modeling of the background may dampen sensitivity in the CATHODE approach, as the weakly-supervised classifier may focus on the differences between the synthetic and true backgrounds rather than identifying signals. However, even with our imperfect background modeling, we have seen strong anomaly detection performance with our chosen signals. We therefore conclude our background model is of sufficiently high quality for the anomaly detection procedure to work, and leave further improvements to future studies.

## V. RESULTS

The performance of the signal classification is expected to vary as a function of the amount of signal present in the dataset. We run the training procedure for several different injection strengths for each signal and evaluate the resulting classification performance. For each injection the procedure is repeated 5 times to assess the stability of results. The injection strength is quantified by the approximate signal significance,  $\sigma = \frac{S}{\sqrt{B}}$ , prior to any additional selection from the anomaly detector. We test injection strengths of  $0.25\sigma$ ,  $0.5\sigma$ ,  $0.75\sigma$ ,  $1\sigma$ ,  $1.5\sigma$ , and  $2\sigma$ . Significance improvement curves (SIC) are used to quantify classification performance. The curves are created by scanning across different classifier thresholds and plotting the signal efficiency divided by the square root of the background efficiency  $\frac{\epsilon_s}{\sqrt{\epsilon_b}}$ , as a function of the background efficiency. The SIC shows the approximate enhancement in signal statistical significance which can be achieved by cutting at a given background efficiency. The achieved classification performance for different signal injections is shown in Fig. 4.

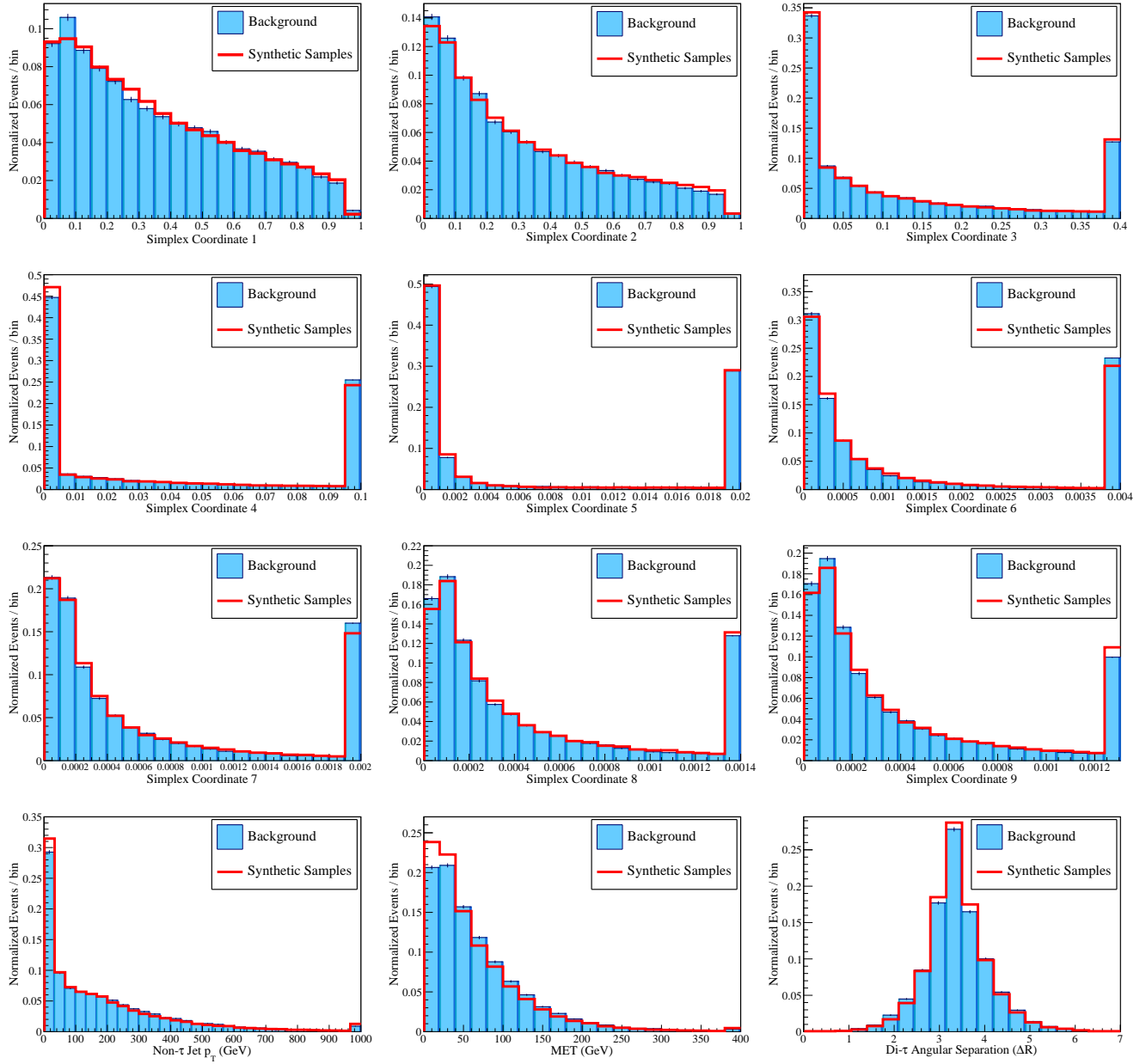


FIG. 3. A comparison of the distributions of true background events in the signal region and the synthetic ones generated by our normalizing flow. Simplex coordinate 10 is omitted for brevity, but has similar distributions. The last bin in each histogram shows overflow entries beyond the range of the histogram axis. The flow is seen to model most of the distributions well. Some discrepancies are seen in the modeling close to variable boundaries at zero.

Figure 5 shows a summary of the anomaly detection performance for the different signal injections. The x-axis denotes the strength of the signal injection and the y-axis the approximate signal significance after the anomaly detection procedure has been performed. The final significance of a signal is estimated as the significance improvement of the anomaly score cut, chosen to have a 1% background efficiency, times the original injection strength. For all three signal models considered, our procedure is able to enhance the signal significance above

the discovery threshold ( $5\sigma$ ) for moderately sized signal injections  $\leq 2\sigma$ . This demonstrates the potential of our anomaly detection approach to discover signals that may have been below the sensitivity threshold of a standard inclusive bump hunt search.

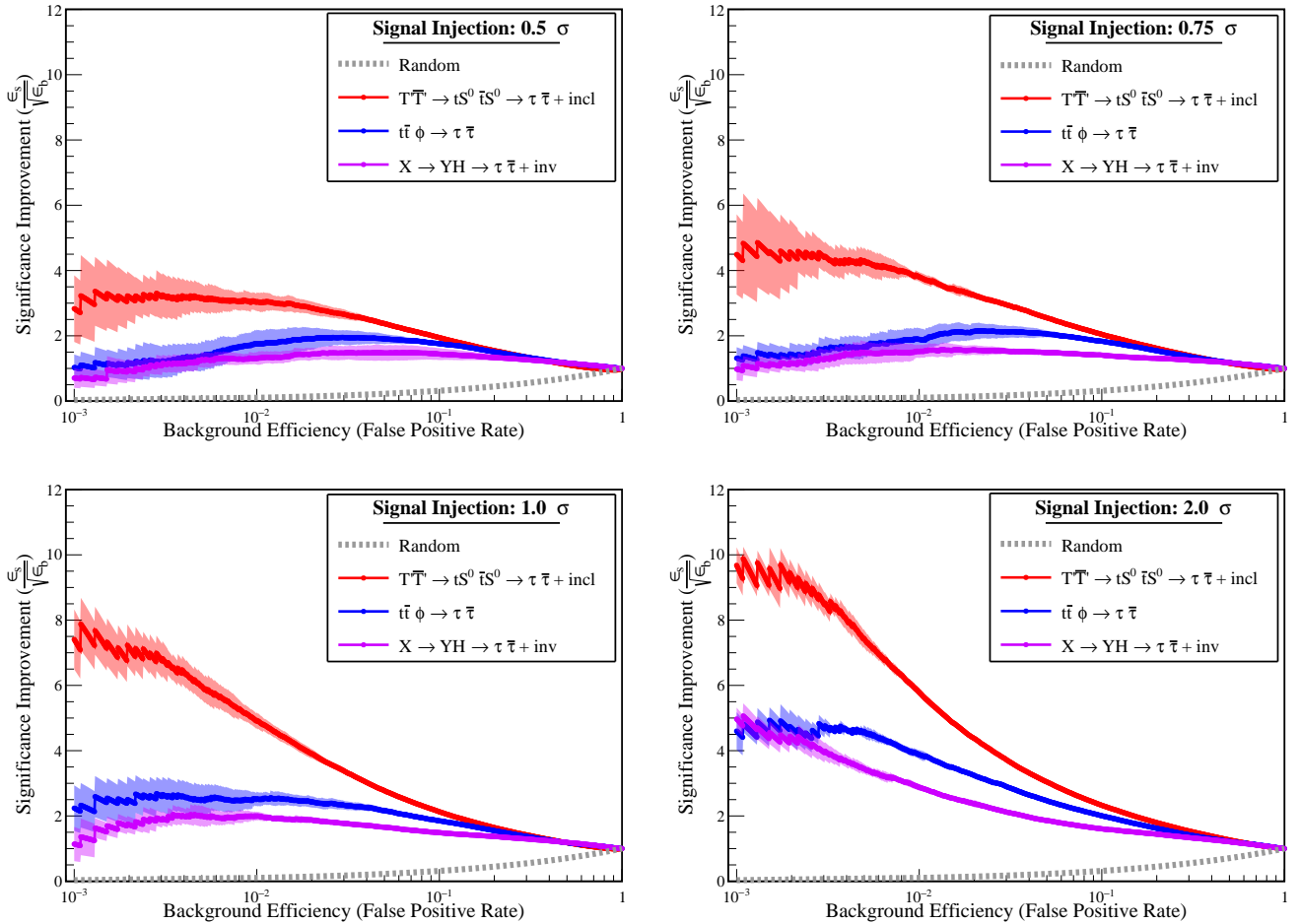


FIG. 4. Significance improvement curves showing classification performance on across our different signal models for signal injections of  $0.5\sigma$  (top left),  $0.75\sigma$  (top right),  $1\sigma$  (bottom left), and  $2\sigma$  (bottom right). The shaded bands represent the statistical uncertainty ( $\pm 1$  standard deviation) in the measured average significance improvement from the 5 different runs.

## VI. CONCLUSION

We have demonstrated the potential for weakly supervised anomaly detection to be applied to a new class of resonance searches. Di-object plus X searches, in which one looks for a resonance decaying to two standard model particles, but produced in association with other anomalous event activity, represents a new class of searches ripe for the application of anomaly detection. In this exploratory work, we focused on a di- $\tau$  plus X final state. We have employed new physically-motivated phase space variables to robustly capture salient features of multi-particle kinematics. We demonstrated that our anomaly detection approach can reach discovery-level significances for signals that would be missed in a conventional bump-hunt approach. Further work can be done to improve the generative modeling of topologically interesting variables like the hypersphere phase space coordinates. We could potentially gain sensitivity from exploring other event-level variables that quantify object type to complement

the kinematic information of the phase space variables. It may be fruitful to explore non-Euclidean normalizing flows, which may better capture the topological features of the phase-space variables, or diffusion models which have been shown to have state of the art performance at physics-based generative tasks [78].

The framework introduced in this paper lays the foundation for a program of searches that can be performed at the LHC with significant discovery potential. Further exploration of topologies suitable for weakly supervised anomaly detection will be essential to deliver on the potential of anomaly detection to transform collider search strategies.

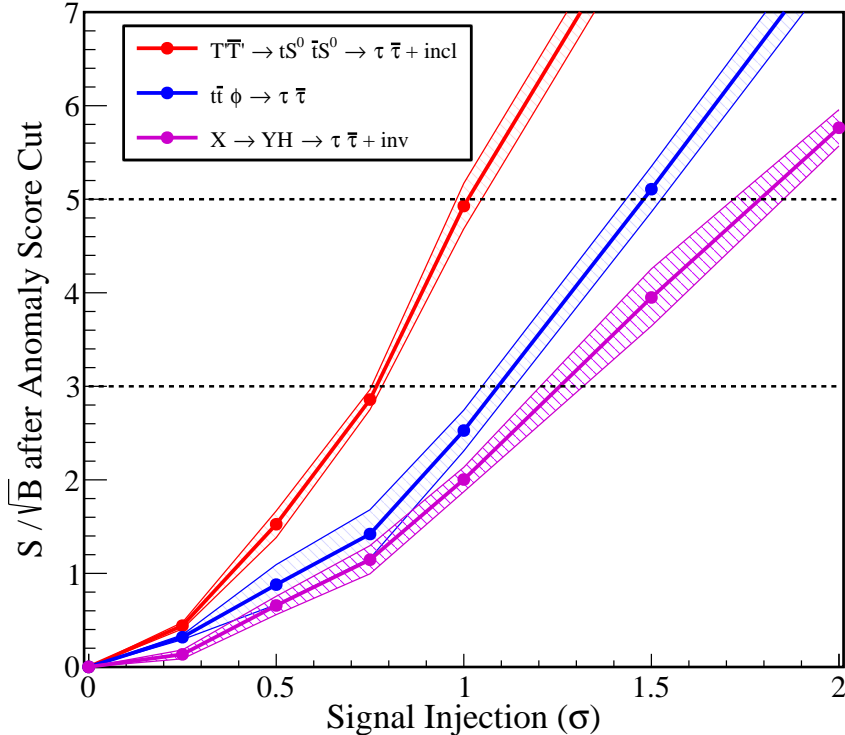


FIG. 5. A summary of the sensitivity enhancement of our anomaly detection approach. The x-axis shows the size of the signal, quantified as  $\frac{S}{\sqrt{B}}$  prior to any anomaly detection selection. The y-axis shows the approximate signal significance achieved after the application of an anomaly score cut that is 1% efficient on the background. Our procedure is able to enhance the signal significance above the discovery threshold ( $5\sigma$ ) for moderately sized signal injections  $\leq 2\sigma$  for all considered signal models.

## ACKNOWLEDGMENTS

We would like to thank Joe Incandela and Nathaniel Craig for useful discussions. We use the `SK_CATHODE` [79] library for implementation. We used the UCSB computational facilities administered by the Center for Scientific Computing at the California NanoSystems Institute and Materials Research Laboratory (an NSF MRSEC; DMR-1720256) and purchased through NSF CNS-1725797. UCSB is supported by the US Department of Energy under grant DE-SC0011702. Support for UCSB is also made possible by the Joe and Pat Yzurdiaga en-

dowed chair in experimental science. LB was also supported by the National Science Foundation Graduate Research Fellowship Program under Grant No. (NSF 2139319). OA is supported by FermiForward Discovery Group, LLC under Contract No. 89243024CSC000002 with the U.S. Department of Energy, Office of Science, Office of High Energy Physics. LM and MS acknowledge support by the Deutsche Forschungsgemeinschaft (DFG, German Research Foundation) under Germany’s Excellence Strategy – EXC2121 “Quantum Universe” – 390833306 as well as by the Bundesministerium für Bildung und Forschung under project 05H24GUA. SS and PM are supported by NSF Grant PHY2310072.

---

[1] G. Kasieczka *et al.*, *Rept. Prog. Phys.* **84**, 124201 (2021), [arXiv:2101.08320 \[hep-ph\]](#).

[2] T. Aarrestad *et al.*, *SciPost Phys.* **12**, 043 (2022), [arXiv:2105.14027 \[hep-ph\]](#).

[3] V. Belis, P. Odagiu, and T. K. Aarrestad, *Rev. Phys.* **12**, 100091 (2024), [arXiv:2312.14190 \[physics.data-an\]](#).

[4] G. Aad *et al.* (ATLAS), *Phys. Rev. Lett.* **125**, 131801 (2020), [arXiv:2005.02983 \[hep-ex\]](#).

[5] ATLAS Collaboration, *Phys. Rev. D* **108**, 052009 (2023), [arXiv:2306.03637 \[hep-ex\]](#).

[6] G. Aad *et al.* (ATLAS), *Phys. Rev. Lett.* **132**, 081801 (2024), [arXiv:2307.01612 \[hep-ex\]](#).

[7] CMS Collaboration, *Reports on Progress in Physics* (2024), [arXiv:2412.03747 \[hep-ex\]](#).

[8] ATLAS Collaboration, *Phys. Review D* (2025), [arXiv:2502.09770 \[hep-ex\]](#).

[9] O. Knapp, O. Cerri, G. Dissertori, T. Q. Nguyen, M. Pierini, and J.-R. Vlimant, *Eur. Phys. J. Plus* **136**, 236 (2021), [arXiv:2005.01598 \[hep-ex\]](#).

[10] R. Gambhir, R. Mastandrea, B. Nachman, and J. Thaler, preprint (2025), [arXiv:2502.14036 \[hep-ph\]](#).

[11] M. Farina, Y. Nakai, and D. Shih, *Phys. Rev. D* (2018), [10.1103/PhysRevD.101.075021](#), [arXiv:1808.08992 \[hep-ph\]](#).

[12] T. Heimel, G. Kasieczka, T. Plehn, and J. M. Thompson, *SciPost Phys.* **6**, 030 (2019), [arXiv:1808.08979 \[hep-ph\]](#).

[13] E. M. Metodiev, B. Nachman, and J. Thaler, *JHEP* **10**, 174 (2017), [arXiv:1708.02949 \[hep-ph\]](#).

[14] J. H. Collins, K. Howe, and B. Nachman, *Phys. Rev. Lett.* **121**, 241803 (2018), [arXiv:1805.02664 \[hep-ph\]](#).

[15] J. H. Collins, K. Howe, and B. Nachman, *Phys. Rev. D* **99**, 014038 (2019), [arXiv:1902.02634 \[hep-ph\]](#).

[16] O. Amram and C. M. Suarez, *JHEP* (2020), [10.1007/JHEP01\(2021\)153](#), [arXiv:2002.12376 \[hep-ph\]](#).

[17] A. Andreassen, B. Nachman, and D. Shih, *Phys. Rev. D* **101**, 095004 (2020), [arXiv:2001.05001 \[hep-ph\]](#).

[18] A. Hallin, J. Isaacson, G. Kasieczka, C. Krause, B. Nachman, T. Quadfasel, M. Schlaffer, D. Shih, and M. Sommerhalder, *Phys. Rev. D* **106**, 055006 (2021), [arXiv:2109.00546 \[hep-ph\]](#).

[19] J. A. Raine, S. Klein, D. Sengupta, and T. Golling, *Front. Big Data* **6**, 899345 (2022), [arXiv:2203.09470 \[hep-ph\]](#).

[20] T. Golling, S. Klein, R. Mastandrea, and B. Nachman, *Phys. Rev. D* **107**, 096025 (2023), [arXiv:2212.11285 \[hep-ph\]](#).

[21] A. Hallin, G. Kasieczka, T. Quadfasel, D. Shih, and M. Sommerhalder, *Phys. Rev. D* **107**, 114012 (2023), [arXiv:2210.14924 \[hep-ph\]](#).

[22] D. Sengupta, S. Klein, J. A. Raine, and T. Golling, *SciPost Phys.* **17**, 046 (2024), [arXiv:2305.04646 \[hep-ph\]](#).

[23] R. Das, G. Kasieczka, and D. Shih, arXiv (2023), [arXiv:2312.11629 \[hep-ph\]](#).

[24] T. Finke, M. Krämer, M. Lipp, and A. Mück, *JHEP* **08**, 015 (2022), [arXiv:2204.11889 \[hep-ph\]](#).

[25] G. Kasieczka, J. A. Raine, D. Shih, and A. Upadhyay, “Complete Optimal Non-Resonant Anomaly Detection,” (2024), [arXiv:2404.07258 \[hep-ph\]](#).

[26] G. Bickendorf, M. Drees, G. Kasieczka, C. Krause, and D. Shih, *Phys. Rev. D* **109**, 096031 (2024), [arXiv:2309.12918 \[hep-ph\]](#).

[27] J. H. Collins, P. Martín-Ramiro, B. Nachman, and D. Shih, *Eur. Phys. J. C* **81**, 617 (2021), [arXiv:2104.02092 \[hep-ph\]](#).

[28] G. Aad *et al.* (ATLAS), *JHEP* (2025), [arXiv:2503.19836 \[hep-ex\]](#).

[29] A. Hayrapetyan *et al.* (CMS), *JHEP* **05**, 311 (2024), [arXiv:2308.07826 \[hep-ex\]](#).

[30] G. Aad *et al.* (ATLAS), *Eur. Phys. J. C* **83**, 1075 (2023), [arXiv:2303.01294 \[hep-ex\]](#).

[31] G. Aad *et al.* (ATLAS), *Phys. Rev. D* **104**, 112005 (2021), [arXiv:2108.07665 \[hep-ex\]](#).

[32] G. Aad *et al.* (ATLAS), *Phys. Rev. Lett.* **125**, 051801 (2020), [arXiv:2002.12223 \[hep-ex\]](#).

[33] A. Tumasyan *et al.* (CMS), *JHEP* **07**, 073 (2023), [arXiv:2208.02717 \[hep-ex\]](#).

[34] B. Capdevila, A. Crivellin, and J. Matias, *Eur. Phys. J. ST* **1**, 20 (2023), [arXiv:2309.01311 \[hep-ph\]](#).

[35] Y. S. Amhis *et al.* (HFLAV), *Phys. Rev. D* **107**, 052008 (2023), [arXiv:2206.07501 \[hep-ex\]](#).

[36] R. Aaij *et al.* (LHCb), *Phys. Rev. Lett.* **115**, 111803 (2015), [Erratum: *Phys. Rev. Lett.* 115, 159901 (2015)], [arXiv:1506.08614 \[hep-ex\]](#).

[37] J. P. Lees *et al.* (BaBar), *Phys. Rev. D* **88**, 072012 (2013), [arXiv:1303.0571 \[hep-ex\]](#).

[38] M. Huschle *et al.* (Belle), *Phys. Rev. D* **92**, 072014 (2015), [arXiv:1507.03233 \[hep-ex\]](#).

[39] S. Hirose *et al.* (Belle), *Phys. Rev. D* **97**, 012004 (2018), [arXiv:1709.00129 \[hep-ex\]](#).

[40] G. Caria *et al.* (Belle), *Phys. Rev. Lett.* **124**, 161803 (2020), arXiv:1910.05864 [hep-ex].

[41] R. Aaij *et al.* (LHCb), *Phys. Rev. D* **97**, 072013 (2018), arXiv:1711.02505 [hep-ex].

[42] R. Aaij *et al.* (LHCb), *Phys. Rev. D* **108**, 012018 (2023), [Erratum: *Phys. Rev. D* 109, 119902 (2024)], arXiv:2305.01463 [hep-ex].

[43] T. A. Vami, “Delphes simulations of different signal models with di-tau final states at the LHC,” (2025).

[44] T. A. Vami, “Datasets used in this paper,” (2025).

[45] L. Brennan *et al.*, “Analysis github repository,” (2025).

[46] T. Finke, M. Hein, G. Kasieczka, M. Krämer, A. Mück, P. Prangchaikul, T. Quadfasel, D. Shih, and M. Sommerhalder, *Phys. Rev. D* **109**, 034033 (2023), arXiv:2309.13111 [hep-ph].

[47] E. Buhmann, C. Ewen, G. Kasieczka, V. Mikuni, B. Nachman, and D. Shih, *Phys. Rev. D* **109**, 055015 (2023), arXiv:2310.06897 [hep-ph].

[48] M. Freytsis, M. Perelstein, and Y. C. San, *JHEP* **02**, 220 (2024), arXiv:2310.13057 [hep-ph].

[49] A. J. Larkoski and T. Melia, *Phys. Rev. D* **102**, 094014 (2020), arXiv:2008.06508 [hep-ph].

[50] T. Cai, J. Cheng, N. Craig, G. Koszegi, and A. J. Larkoski, *JHEP* **09**, 054 (2024), arXiv:2405.16698 [hep-ph].

[51] J. Alwall, R. Frederix, S. Frixione, V. Hirschi, F. Maltoni, O. Mattelaer, H. S. Shao, T. Stelzer, P. Torrielli, and M. Zaro, *JHEP* **07**, 079 (2014), arXiv:1405.0301 [hep-ph].

[52] L. Darmé *et al.*, *Eur. Phys. J. C* **83**, 631 (2023), arXiv:2304.09883 [hep-ph].

[53] T. Sjöstrand, S. Ask, J. R. Christiansen, R. Corke, N. De-sai, P. Ilten, S. Mrenna, S. Prestel, C. O. Rasmussen, and P. Z. Skands, *Comput. Phys. Commun.* **191**, 159 (2015), arXiv:1410.3012 [hep-ph].

[54] R. D. Ball, L. Del Debbio, S. Forte, A. Guffanti, J. I. Latorre, J. Rojo, and M. Ubiali, *Nucl. Phys. B* **838**, 136 (2010), arXiv:1002.4407 [hep-ph].

[55] R. D. Ball *et al.* (NNPDF), *JHEP* **04**, 040 (2015), arXiv:1410.8849 [hep-ph].

[56] FeynRules Database, “The Standard Model,” <https://feynrules.irmp.ucl.ac.be/wiki/StandardModel> (2018).

[57] J. Alwall *et al.*, *Eur. Phys. J. C* **53**, 473 (2008), arXiv:0706.2569 [hep-ph].

[58] P. Artoisenet, R. Frederix, O. Mattelaer, and R. Rietkerk, *JHEP* **03**, 015 (2013), arXiv:1212.3460 [hep-ph].

[59] FeynRules Database, “Two-Higgs-Doublet Model (2HDM),” <https://cp3.irmp.ucl.ac.be/projects/feynrules/wiki/2HDM> (2018).

[60] G. C. Branco, L. Lavoura, and J. P. Silva, *CP Violation*, Vol. 103 (Oxford University Press, 1999).

[61] C. Degrande, *Comput. Phys. Commun.* **197**, 239 (2015), arXiv:1406.3030 [hep-ph].

[62] FeynRules Database, “Vector like quarks + exotic pNGBs,” [https://feynrules.irmp.ucl.ac.be/raw-attachment/wiki/NLOModels/eVLQ\\_v8.1.tar.gz](https://feynrules.irmp.ucl.ac.be/raw-attachment/wiki/NLOModels/eVLQ_v8.1.tar.gz) (2016).

[63] A. Banerjee *et al.*, “Phenomenological aspects of composite Higgs scenarios: exotic scalars and vector-like quarks,” (2022), arXiv:2203.07270 [hep-ph].

[64] FeynRules Database, “The Next-To-Minimal Supersymmetric Standard Model,” <https://cp3.irmp.ucl.ac.be/projects/feynrules/wiki/NMSSM> (2018).

[65] U. Ellwanger, C. Hugonie, and A. M. Teixeira, *Phys. Rept.* **496**, 1 (2010), arXiv:0910.1785 [hep-ph].

[66] A. Djouadi *et al.*, *JHEP* **07**, 002 (2008), arXiv:0801.4321 [hep-ph].

[67] P. Z. Skands *et al.*, *JHEP* **07**, 036 (2004), arXiv:hep-ph/0311123.

[68] B. C. Allanach *et al.*, *Comput. Phys. Commun.* **180**, 8 (2009), arXiv:0801.0045 [hep-ph].

[69] I. Bigaran, B. A. Dobrescu, and A. Russo, *Phys. Rev. D* **109**, 055033 (2024), arXiv:2312.09189 [hep-ph].

[70] M. J. Baker, J. Fuentes-Martín, G. Isidori, and M. König, *Eur. Phys. J. C* **79**, 334 (2019), arXiv:1901.10480 [hep-ph].

[71] B. Kayser and R. E. Shrock, *Phys. Lett. B* **112**, 137 (1982).

[72] J. de Favereau, C. Delaere, P. Demin, A. Giammanco, V. Lemaître, A. Mertens, and M. Selvaggi (DELPHES 3), *JHEP* **02**, 057 (2014), arXiv:1307.6346 [hep-ex].

[73] M. Cacciari, G. P. Salam, and G. Soyez, *Eur. Phys. J. C* **72**, 1896 (2012), arXiv:1111.6097 [hep-ph].

[74] A. M. Sirunyan *et al.* (CMS), *JINST* **13**, P10005 (2018), arXiv:1809.02816 [hep-ex].

[75] A. Tumasyan *et al.* (CMS), *JINST* **17**, P07023 (2022), arXiv:2201.08458 [hep-ex].

[76] G. Papamakarios, E. Nalisnick, D. J. Rezende, S. Mohamed, and B. Lakshminarayanan, *Journal of Machine Learning Research* (2021), arXiv:1912.02762 [stat.ML].

[77] F. Pedregosa, G. Varoquaux, A. Gramfort, V. Michel, B. Thirion, O. Grisel, M. Blondel, A. Müller, J. Nothman, G. Louppe, P. Prettenhofer, R. Weiss, V. Dubourg, J. Vanderplas, A. Passos, D. Cournapeau, M. Brucher, M. Perrot, and Édouard Duchesnay, “Scikit-learn: Machine learning in python,” (2018), arXiv:1201.0490 [cs.LG].

[78] O. Amram *et al.*, “CaloChallenge 2022: A Community Challenge for Fast Calorimeter Simulation,” (2024), arXiv:2410.21611 [physics.ins-det].

[79] M. Sommerhalder *et al.*, “SK CATHODE Github Repo,” (2025).

[80] D. P. Kingma and J. L. Ba, “Adam: A method for stochastic optimization,” (2017), arXiv:1412.6980 [cs.LG].

## Appendix: Implementation Details

### 1. Preprocessing

The **Delphes** files generated in Section III are further processed before being utilized with CATHODE. A luminosity under sampling is applied so the effective luminosity of the background samples is scaled to match the  $138 \text{ fb}^{-1}$  collected data in LHC Run-2. A random selection of events with yield as detailed in the upper section of Table II are used for analysis. After under sampling, the two simulated background datasets are combined and preprocessed following the cuts discussed in Section IV, with the resulting event distributions shown in the lower section of Table II.

In the CATHODE method, the synthetic background samples generated by the normalizing flow should be in-

Name	#Events	Lumi-scaled #events
Drell-Yan $\tau\bar{\tau}$	3M	2,397,067
$t\bar{t}$	2M	1,861,869
Combined Lumi-scaled		After cuts
Drell-Yan + $t\bar{t}$	4,258,936	$\sim 158,000$

TABLE II. Number of events before and after luminosity under sampling (top). Event counts before and after preprocessing cuts (bottom).

distinguishable from the true background events in the SR. If this is not the case, then the weakly supervised classifier will fail to learn to identify the signal, instead learning to distinguish the real and synthetic background events. The use of phase space variables, which have a distinct topological structure and complex interdependence, made this non-trivial to achieve.

A key challenge in the feature engineering was the handling of zero-padded object coordinates in the phase space. Because of normalization conditions, the phase-space simplex variables of the zero-padded objects have a distinct non-zero value that is exactly the same for all objects in the event, but the value varies between events due to a dependence on the other event objects. This strict non-trivial structure is very difficult for the normalizing flow to model exactly. Without proper preprocessing, we found that a classifier would trivially distinguish between real and synthetic background events based on very small variations in this regularity, undermining the CATHODE methodology.

We implemented a stochastic noise addition procedure that carefully applied a small amount of Gaussian noise (approximately 1% of the coordinate magnitude) to the simplex coordinates of padded objects. This technique effectively blurred these strict regular features of the zero-padded objects, allowing for high-quality modeling by the generative model, without distorting the overall distribution characteristics.

Following this noise addition, we employ a sequence of transformations to optimize the feature space for normalizing flows. First, all features are shifted and scaled to the range  $x \in (0, 1)$ . Then a logit transformation ( $\text{logit}(x) = \ln\left(\frac{x}{1-x}\right)$ ) is applied to convert bounded domains into unbounded ones. The transformed features are then standardized by subtracting the mean and dividing by the standard deviation of the training set, respective to each feature. This preprocessing pipeline ensures that the normalizing flow operates on a well-conditioned feature space while preserving the essential structure of the phase space manifold.

Simulated and synthetic data in the signal and sideband regions are further split into train-

ing/validation/testing datasets following the methods described in Section IV. The corresponding event counts can be seen in Table III.

Name	Total # of Events	Sideband	Signal Region
Drell-Yan + $t\bar{t}$	$\sim 158,000$	$\sim 127,000$	$\sim 31,000$
	Training	Validation	Testing
Sideband	89,000	38,000	-
Signal Region	13,000 Simulated 39,000 Synthetic	13,000 Simulated 39,000 Synthetic	5,000 Background 5,000 Signal

TABLE III. Numbers of events used for training, validation, and testing in the signal region and sidebands (rounded to the nearest thousand).

## 2. Generative Model

Our generative model is based on a normalizing flow architecture. It consists of 6 layers of a spline-based masked piecewise rational quadratic autoregressive flow [76]. Each layer uses 6 MADE blocks, a hidden feature size of 512, 24 bins, and a tail bound of 6. The flow is trained with a learning rate of  $5 \times 10^{-5}$  using the Adam optimizer [80] and a batch size of 256. The model is trained until the validation loss fails to improve for 50 epochs.

The flow is trained on events from the sideband regions, conditioning on the di- $\tau$  visible invariant mass. The flow learns a bijective, invertible mapping  $z = f(\vec{x}; m_{vis})$  between the feature space  $x$  and a latent space  $z$  following a simple base distribution (unit normal). The power of this approach is that once trained, the inverse function  $\vec{x} = f^{-1}(z; m_{vis})$  can be queried for any mass value  $m_{vis}$ , including those in the SR.

After training, we select the model state with the lowest validation loss for the subsequent interpolation and sampling steps.

To learn the di- $\tau$  mass distribution in the SR, we utilize a kernel density estimate (KDE) implemented from the `scikit-learn` library [77]. We use a Gaussian kernel with a bandwidth of 0.01. The KDE is fit to the mass distributions in the sideband training set and then a mass distribution for the SR is generated.

To generate synthetic background events in the SR, we first sample mass values from a kernel density estimate of the SR mass distribution. We then draw samples from the base distribution  $z \sim \mathcal{N}(0, 1)$ . The inverse transformation  $\vec{x} = f^{-1}(z; m_{vis})$  learned by our flow is then applied to generate synthetic background events.

Since the normalizing flow operates on transformed features, we apply the inverse of the standardization and logit transformation to convert the sampled events back to physical space.